INL/EXT-18-51683
Revision 1

Transient Coupled Chemical-Thermal-Fluid Field Simulation for Sealed Aluminum-clad Spent Nuclear Fuel Storage Canister

Alexander Abboud

Hai Huang

December 23rd, 2020

The INL is a U.S. Department of Energy National Laboratory
operated by Battelle Energy Alliance

INL/EXT-18-51683
Revision 1

Transient Coupled Chemical-Thermal-Fluid Field Simulation for Sealed Aluminum-clad Spent Nuclear Fuel Storage Canister

December 23rd, 2020

Idaho National Laboratory
PO Box 1625
Idaho Falls, Idaho 83415

http://www.inl.gov

Prepared for the
U.S. Department of Energy
Office of Environmental Management
Under DOE Idaho Operations Office
Contract DE-AC07-05ID14517

Executive Summary

As the first step toward developing three-dimensional (3D) multi-physics computational fluid dynamics (CFD) model for unsealed and vented canister storage system, a 3D CFD model coupled with bulk gas radiolysis reactions was developed first for sealed DOE standard canisters filled with inert gas and trace amount of air and water. The workflow for constructing canister-scale 3D CFD models and coupling with gas phase radiolysis reactions were established, which can be readily extended to unsealed, vented canister storage system. This interim milestone report documents the theory of the model, workflow to establish radiolysis reaction network, and initial simulations of the evolutions of thermal fields and hydrogen gas concentrations within sealed DOE standard canisters over long period of time. In addition, a mesh refinement test was done to show that increasing the models mesh refinement had negligible impact upon the temperature profiles.

(Page left blank)

Acknowledgements

This work was funded by the U.S. Department of Energy Environmental Management office. This work was performed by Battelle Energy Alliance, LLC, under DOE Idaho Operations Contract DE-AC07-05ID14517.

(Page left blank)

List of Acronyms

ATR	Advanced Test Reactor
CFD	Computational Fluid Dynamics
CFL	Courant-Friedrichs-Lewy
DOE	Department of Energy
INL	Idaho National Laboratory
SNF	Spent Nuclear Fuel

Table of Contents

List of Figures

List of Tables

1. INTRODUCTION

Fuel storage at the Idaho National Laboratory (INL) is slated to last at least 50 years given the current prospects for long term repository in the United States. To adapt to the new storage requirement, further understanding of the fuel storage canisters is required. This includes not only the thermal fields, as many past computational fluid dynamics (CFD) studies have looked into for commercial fuel, but also the buildup of species due to the radiolytic chemical reactions.

The flow in storage containers of spent nuclear fuel is primary driven through natural convection as air is heated from the central fuel and cooled by the outer air (Nishimura et al. 1996; Lee et al. 2000; Lee 2013; Heng et al. 2002). Serval experimental studies have characterized the flow field and temperatures for commercial fuel storage casks (Bang et. al 2015; Jeong et al 2016; Smith 2016; Takeda 2008). Prior modeling of thermal fields and convective patterns with computational fluid dynamics (CFD) have focused on steady state simulations timed for either early or late into the storage cycle (Lee et al. 2000; Li 2016 et al.; Yoo 2010 et al.; Lee 2009 et al.; Povskas 2017 et al.; Brewster 2012 et al.; Kim 2014 et al.; Tseng 2011 et al.; Herranz 2015 et al., Wu et al. 2018). Sensitivities to the parameters of the SNF storage have been studied in these systems for peak cladding temperature to ensure no melting of the plating occurs (Herranz et al. 2015; Kim 2014 et al.). Improvements to basic models have used commercial packages to fully resolve the fuel configurations in lieu of coarse-resolution porous media models (Brewster et al. 2012). However, past CFD models have not coupled the thermal and convective fields with the chemical species which occur due to the radiolytic breakdown of water vapor that can be present in the storage containers due to chemisorption on fuel plating or residual water after backfilling (Wittman and Hanson 2015; Arkhipov 2007; Atkinson 2004). In addition, the past CFD models have not looked at the transient evolution of the thermal fields inside canisters, opting for steady state solutions.

This study looks into the methods of coupling the thermal and velocity fields developing over time within a fully packed and sealed DOE standard canister with ATR fuel that is coupled with the complex radiolytic chemistry system in a transient model to determine buildup of the gases (e.g., H_2 in particular of interest) over a long-term storage period. This then considers a sensitivity case to examine this output based

on fuel stored initial decay heat, initial residual water, outer canister temperature, emissivity of outer canister, and internal canister pressure. The development of the coupled CFD with radiolysis chemistry model for sealed canister storage system is the first step toward developing multiphysics CFD models for unsealed, vented canister storage system using Idaho National Laboratory (INL) INTEC CPP-603 facility as an example.

2. THEORY AND MODEL DESCRIPTION

The primary sources for the development of the geometries for the DOE sealed canister model as well as information to determine the bounds for the initial conditions to be used in the model is primarily from three reports:

- Lockheed Martin Idaho Technologies Co, Aug 1998. Preliminary design specification for Department of Energy standardized spent nuclear fuel canisters Volume 1: Design specification (DOE/SNF/REP--011-Vol 1). Tech. Rep. Idaho National Engineering and Environmental Lab, Idaho Falls, ID (United States).
- Kim, S. S., Pope, C., Taylor, L. L., et al., 2007. Criticality analysis for proposed maximum fuel loading in a standardized snf canister with type 1a baskets, INL/EXT-07-12326. Tech. rep., Idaho National Laboratory, Idaho Falls, ID (United States).
- Wertsching A., et al., Material Interactions on Canister Integrity During Storage and Transport, DOE/SNF/REP-104, 2007.

2.1 Thermal-Fluid Model

The commercial multiphysics modeling platform STAR-CCM+ is used for modeling the canister (Siemens, 2017). The numerical solver implemented here is a finite-volume approach with second-order implicit time stepping and a second-order discretization scheme. The segregated flow solver for the Navier-Stokes equations is used, which is applicable to constant density or mildly compressible flows, with a predictor-corrector approach that couples the momentum and continuity equations. A collocated variable arrangement with a Rhie-Chow scheme for pressure-velocity coupling is implemented in a SIMPLE-type algorithm (Siemens, 2017). Due to the low value of the Reynolds number, a laminar model is used based on the assumption that the solution is a fully resolved laminar flow. The momentum equation is then given by

$$\frac{\partial(\rho \mathbf{v})}{\partial t} + \nabla \cdot (\rho \mathbf{v} \otimes \mathbf{v}) = -\nabla \cdot (p\mathbf{I}) + \nabla \cdot \mathbf{T} + \mathbf{f}_b \quad (1)$$

Where $\mathbf{v}$ is the velocity vector, and ρ is the density. The $\boldsymbol{f}_b$ term is the body force, solely occurring due to the buoyancy driven flow in this case. The viscous stress tensor is

$$T = \mu(\nabla \mathbf{v} + (\nabla \mathbf{v})^T) - \frac{2}{3}\mu(\nabla \cdot \mathbf{v})\mathbf{I} \quad (2)$$

Where μ is the air viscosity. The mass conservation is expressed through the continuity equation

$$\frac{\partial \rho}{\partial t} + \nabla \cdot (\rho \mathbf{v}) = 0 \quad (3)$$

The conservation of energy gives an equation in terms of the total energy, E, as

$$\frac{\partial(\rho E)}{\partial t} + \nabla \cdot (\rho E \mathbf{v}) = \mathbf{f}_b \cdot \mathbf{v} + \nabla \cdot (\mathbf{v} \cdot \boldsymbol{\sigma}) - \nabla \cdot q + S_E \quad (4)$$

Where in the solid phases, the terms with $\mathbf{v}$ are equal to 0, q is the conductive heat flux, the energy source term S_E is due to the chemical reactions in the fluid phase, and is from the specified heat source for the fuel plates in that solid region. The implicit solver in STAR-CCM+ can typically adapt up to a Courant-Friedrichs-Lewy (CFL) condition of nearly 50. The properties for the materials used for each of the solid regions are shown in Table 1, it is assumed maximum temperatures are low enough to use constant thermal properties for solids.

Table 1. *Physical properties of the components of the DOE standard canister.*

Material	Density [kg/m3]	Thermal Conductivity [W/m K]	Heat Capacity [J/kg K]	Emissivity [-]
Al-6061 (siding/back plates) (Polkinhorne, 1991)	2702	167	896	0.82
Stainless Steel 304 (Type 1a basket) (Incropera et al. 2007)	7900	14.9	477	0.22 (clean) 0.70 (oxidized)
Stainless Steel 316 (DOE standard canister) (Incropera et al. 2007)	8238	13.4	468	0.22 (clean) 0.70 (oxidized)
Carbon Steel (impact plate) (Incropera et al. 2007)	7854	60.5	434	0.89
ATR Fuel Plates (Ilum 1996)	3680	42.6	614.0	0.82 (assumed)

For the worst case scenario, consider that the ventilation to the facility is shut off and no flow external to the canisters is present, then the heat transfer coefficient is calculated from the effect of heat gradient buoyancy driven flow. For a vertical heated plate, the Nusselt number, *Nu*, is given by

$$Nu = \left\{ 0.825 + \frac{0.387\, Ra_L^{1/6}}{\left[1 + \left(\frac{0.492}{Pr}\right)^{\frac{9}{16}}\right]^{8/27}} \right\}^2 \tag{5}$$

Where the Prandtl number, *Pr*, is evaluated for the gas, and the Rayleigh number, *Ra*, based on the height, L, is given by

$$Ra_L = \frac{g\mathrm{B}(T_s - T_\infty)L^3}{\nu\alpha} \tag{6}$$

Where B is the thermal expansion coefficient, and α is the thermal diffusivity. A slightly modified correlation to this for heated horizontal plates is used for the canister top surface. For calculation of the exterior heat loss conditions for the Nusselt numbers, temperature dependent thermal properties for air from Incorpera et al. are used. In addition to convective heat loss, radiative heat losses from the canisters are considered with emissivity values of stainless steel for DOE standard canisters.

2.2 Chemical Equations

The chemical reactions which are considered are one-step irreversible reactions. From Wittman & Hanson, 2015, the list considered here is in the event that the sealed canisters have been entirely backfilled with helium, and a negligible amount of air present. The initial water vapor for the system could be from initial residual water or from the evolution of water chemisorbed into the ATR aluminum layers which may enter the gas phase over time.

Following the full set of model reactions from Wittman & Hanson, 2015, a model was developed from literature for a full set of chemical reactions using prior experimental collection of radiolysis data (Bulearca et al., 2010, Atkinson et al., 2004; Arkhipov et al., 2007). For the initial model consider the sealed DOE standard canister case. The maximum heat output is set at 1500 W, and from initial thermal modeling,

the expected maximum temperature is 104 °C. The reaction model described out by Wittman & Hanson, 2015, considers the full radiolysis reactions and recombination reactions for a system containing helium, air and water vapor, with trace amounts of CO2. This amounts to 115 total reactions (where 4 are radiolytic decomposition) among 40 different chemical species and intermediate molecular radicals.

For the sealed canister we consider the simplified reaction network, where no air is present after the vacuum process, and the only initial gases are helium and trace water vapor. From the full set of equations, then any equation containing N or C is disregarded, which eliminates more than half of the equations. Elimination of trace amounts of ozone eliminates another 5 reactions. If it is considered that no charged molecules can be present for long periods of time, then reactions involving H_2O+, H_3O+, as well as e- and $O+$, O_2+ are also eliminated, the reactions involving these charged species do not compete so no side end reactions would be expected as a result of ignoring these. This results in a reduction of this full mechanism to 22 chemical reactions with 2 radiolytic decomposition reactions, containing a total of 8 species. The species considered are: He, H_2O, H_2O_2, HO_2, O_2, H_2, H, OH and O. The radiolysis reactions are given by

$$7.35\ \mathrm{H_2O} \rightarrow 7.4\ \mathrm{H}\cdot + 6.3\mathrm{OH}\cdot + 0.5\mathrm{H_2} + 1.05\mathrm{O},$$

and

$$5.3\mathrm{O_2} \rightarrow 5.23\mathrm{O}\cdot + 2.07\mathrm{O_2^+} + 1.23\mathrm{O^+} + 3.3\mathrm{e^-}.$$

Although with the assumption to disregard charged molecules the second radiolysis reaction simplifies to

$$3.23\mathrm{O_2} \rightarrow 6.46\mathrm{O}\cdot$$

The chemical species are modeled as a combination of the radiolytic reactions and the recombination reactions where the source term in terms of concentration is

$$\frac{d[A_i]}{dt} = \dot{d}\sum G_i w_g[A_g] + \sum k_{ir}\prod[A_{jr}]^{O_{jr}} \tag{7}$$

Where $\dot{d}$ is the dose rate, G_i is the G-value for the radiolytic decomposition, w_g is the molecular weight, k_{ir} is the reaction rate, and O_{jr} is the reaction order for species j. The transport equations for the species mass fractions, Y_i, are solved for N-1 species in the CFD model as

$$\frac{\partial \rho Y_i}{\partial t} + \nabla \cdot (\rho v Y_i) = \nabla \cdot \left(J_i + \frac{\mu_t}{\sigma_t} \nabla Y_i \right) + S_{Y_i} \tag{8}$$

The source term here, S_{Y_i}, is reformulated from equation 7 to be in terms of the mass fractions rather than concentration. The basic diffusion is defined as

$$J_i = \rho D_{i,m} \nabla Y_i \tag{9}$$

Where $D_{i,m}$ is the binary diffusion coefficient. The general reaction term is defined as

$$k_{ir} = k_{ir}^0 T^{x_r} \exp\left(-\frac{E_r}{T}\right) \tag{10}$$

where the universal gas constant has been lumped into the activation energy, E_r. The coefficients for each reaction, k_{ir}^0, x_r and E_r are listed in Table 2 for each reaction considered. Each listed reaction is only considered to be a forward one-step reaction.

Cantera software was used (Goodwin et al., 2018) to process the full set of chemical reactions provided by Wittman & Hanson (2015) in order to perform reaction network reduction through sorting the lowest chemical rates relative to others. Reduction was done until the set of reactions no longer produced the same hydrogen output over a long batch simulation. Reactions that were deemed unnecessary were removed, and the entire new mechanism was run though Cantera again to confirm that the reduced mechanism resulted in the same mole fractions for all of the major species in less than 1% error. This process was repeated until the minimum threshold of reactions to keep in the mechanism was determined, the simplified chemical mechanism is shown in Table 2. The plot of the hydrogen concentration vs. time outputted for a range of chemical reactions kept in the mechanism is shown in Figure 1a. This is generated at 100C with 1% residual H2O and 99% Helium by moles for the initial condition. Reducing the full set to a fraction of the reactions – from 5 to 10 – can show an overprediction in the generated hydrogen due to the lack of competing reactions. At a reduction to 14 total chemical reactions, the reduced mechanism shows agreement with under 1% error in the hydrogen generation rate over a long period of time. The full set of chemical species in the model is plotted over time in Figure 1b for the full mechanism, and is plotted in

Figure 1c for the reduced mechanism with 14 reactions. The agreement is quite strong across all of the species except for H_2O_2, which is off by about 15%. However, the total amount of H_2O_2 which exists at the equilibrium state is quite small, and it would likely be inconsequential to ignore this difference for a trace species.

Table 2. *List of chemical reactions for the reduced chemical mechanism.*

K_{ir}^0	x_r [-]	E_r [1/K]	Reaction
1.69e11	0	4.420e2	$H\cdot + HO_2 \rightarrow 2OH\cdot$
2.55e10	0	7.0e2	$H\cdot + HO_2 \rightarrow H_2O + O\cdot$
1.20e11	0	0	$HO_2 + OH\cdot \rightarrow H_2O + O_2$
1.0e13	-1	0	$2H\cdot + H_2O \rightarrow H_2O + H_2$
1.4e17	-2	0	$H\cdot + OH\cdot + H2O \rightarrow 2H_2O$
6e16	-2	0	$2OH\cdot + H_2O \rightarrow H_2O_2 + H_2O$
8.91e9	0	2.5e2	$O\cdot + OH\cdot \rightarrow O_2 + H\cdot$
1.56e12	-0.8	0	$H\cdot + O2 + H_2O \rightarrow H_2O + HO_2$
2.39e10	0.09	7.1e2	$H\cdot + HO_2 \rightarrow H_2 + O_2$
4.46e9	0	4.77e2	$OH\cdot + H_2O_2 \rightarrow H_2O + HO_2$
2.53e5	0.48	1.70e3	$OH\cdot + H_2 \rightarrow H_2O + H\cdot$
1.5e6	1.14	5.0e1	$2OH\cdot \rightarrow H_2O + O\cdot$
2.51e15	0	2.41e4	$H_2O_2 + H_2O \rightarrow 2OH\cdot + H_2O$
1e7	0	5e3	$H\cdot + H_2O \rightarrow H_2 + OH\cdot$

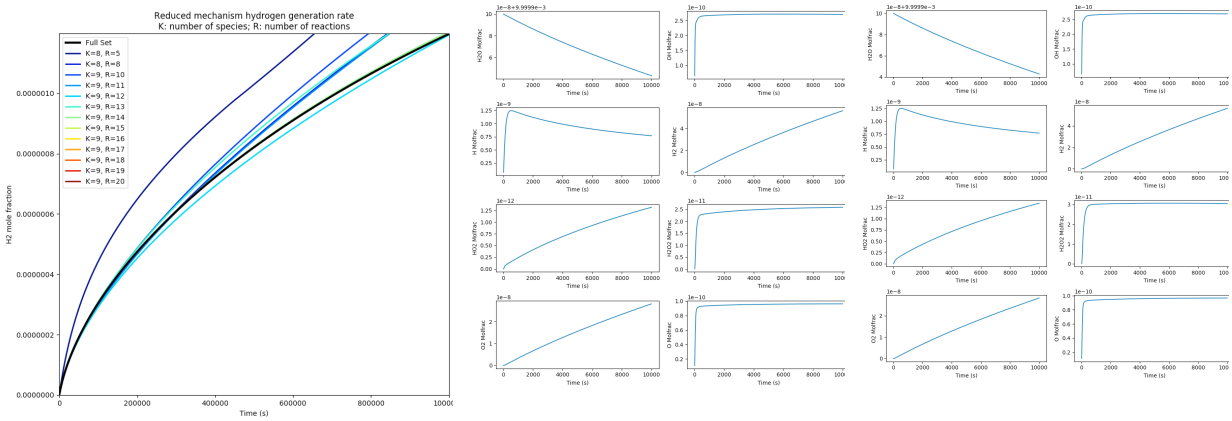

(a) (b) (c)

Figure 1. The (a) long-term evolution of hydrogen for various numbers of reactions in a reduced mechanism. Evolution of all chemical species for the (b) full mechanism in Cantera, and for the (c) reduced mechanism.

2.2.1 Reaction Pathway

The full reaction pathway for the Wittman system of chemical equations for each element present is shown in Figure 2a-d, for H, C, O, and N, respectively. These were created through tabulated and sorting the

reaction rates of each species using Cantera (Goodwin et al. 2017). The reaction pathway for the reduced system of chemical equations used in the mechanism implemented in the CFD code is shown in Figure 3a-b - though it only includes H & O, as air was neglected. The reaction pathways are based on the rates at 10 hours of simulated time at 100 C, shifting of the magnitudes will occur over time as equilibrium is reached.

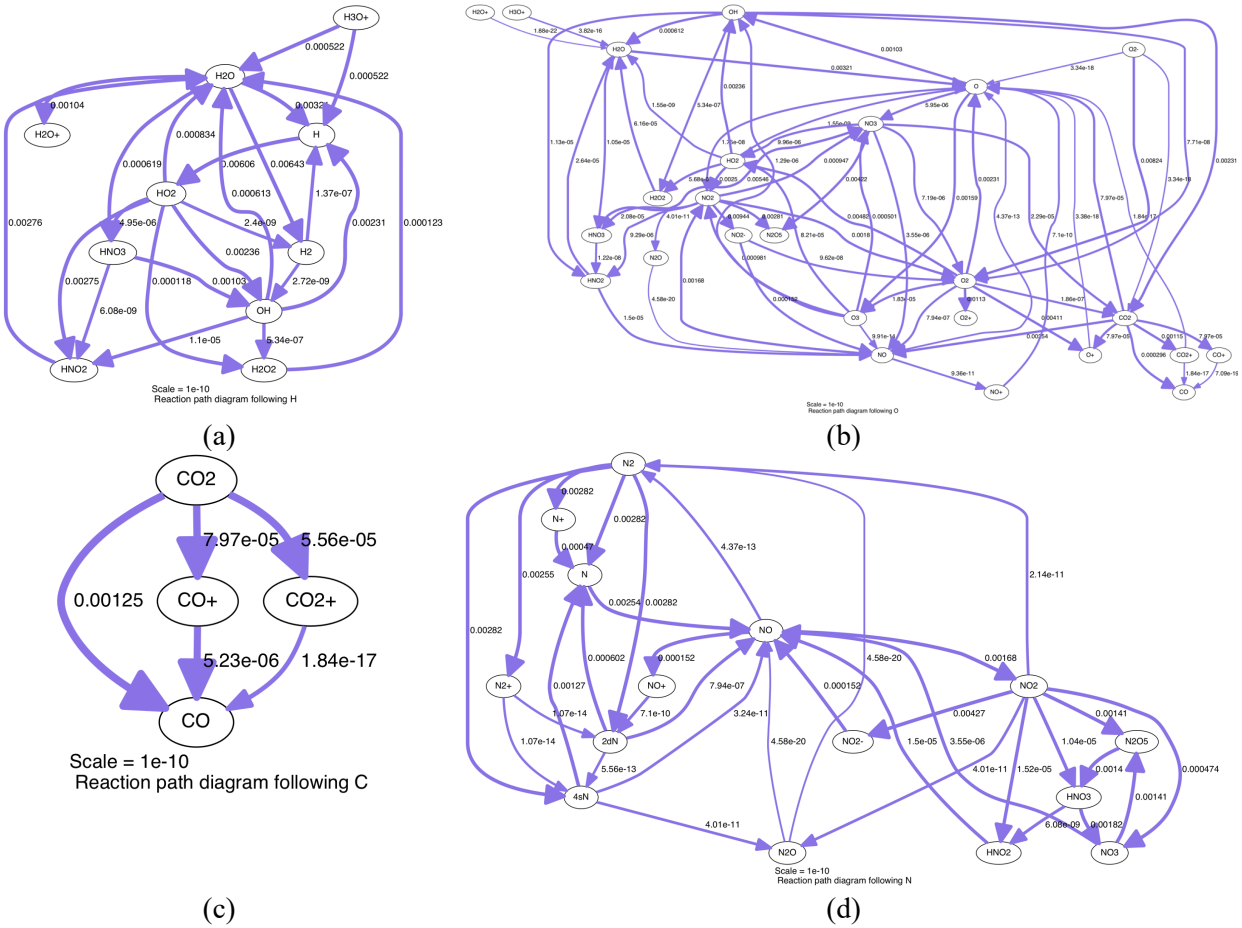

Figure 2. Reaction pathway of (a) H, (b) O, (c) C, and (d) N for the full set of chemical reaction specified in Wittman and Hanson, 2015.

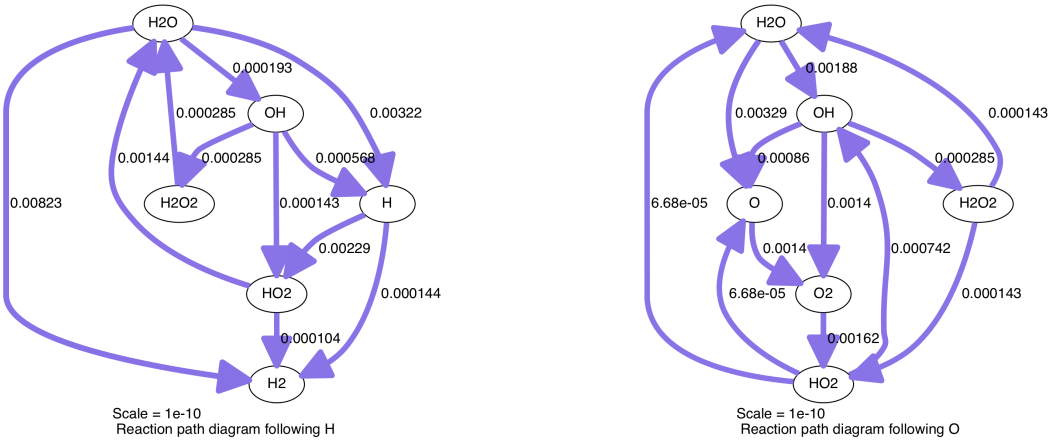

(a) (b)

Figure 3. Reaction pathway of (a) H and (b) O for the reduced set of chemical reactions in the sealed canister model.

2.3 Model Geometry of Sealed DOE Standard Canister and Mesh Generation

The geometry for a packed ATR fuel canister is described in Kim et al., 2007, with additional information in (DOE-REP-90). The canister is a standard DOE canister 15 foot long with a diameter of 18 inches made of stainless steel 316, inside the canister are 3 Type1a baskets (shown in Figure 4a-d) made of stainless steel 304. Inside each Type1a basket is 10 ATR fuel assembles. The quarter canister with symmetry conditions is used to improve computational time for the model, with the fuel plates and air gaps between the plates the fully resolved the model contains 5 million cells. Slices of the canister with the mesh for the horizontal and vertical directions are shown in Figure 4e and 2f, respectively. Here the red denotes fuel plates, blue is the air region, light grey is the aluminum side and back plates, medium grey is the Type 1a basket, and dark grey is the DOE canister.

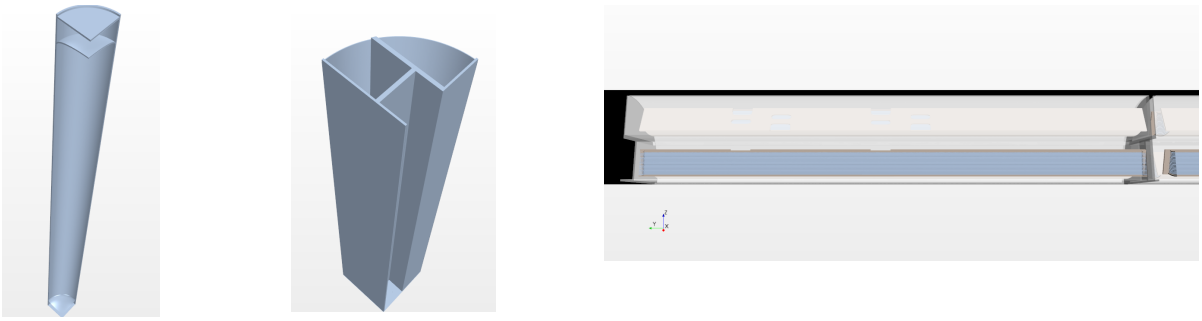

(a) (b) (c)

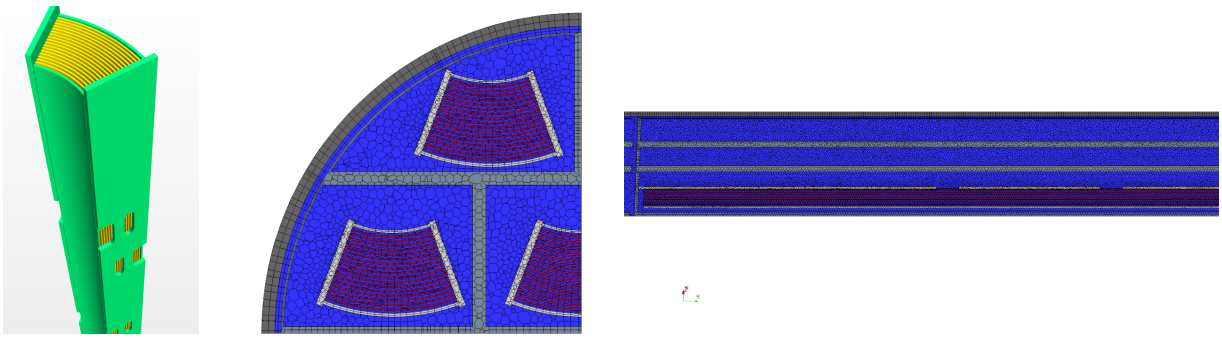

(d) (e) (f)

Figure 4. Quarter domain of (a) canister geometry, (b) type 1a basket, (c) load canister, (d) ATR fuel element, and (e) horizontal mesh slice, (f) vertical mesh slice.

2.4 Thermal Decay Heat and Ambient Conditions

Ambient temperatures for the INL INTEC CPP-603 facility are described in Christensen (2003a,b). Due to the lack of long-term geological storage facility, it is considered that the canisters modeled here would be placed in a extended storage facility with the same characteristics of INL INTEC CPP-603. A plot of the ambient temperature conditions measured when the facility had working thermocouples in 2011 is shown in Figure 5, with 9 thermocouples, these are recorded once per hour. This is broken down further showing the trend over a single week, and showing the whole data set in week long increments. The ambient temperature within the facility itself has a very small variation within it compared to the exterior climate due to the large amount of mass of spent fuel stored within it. The largest temperature difference in a 12 hour span is only 1.5° C, and largest temperature difference in a week-long span is 4.4° C. The difference from the average for the minimum and maximum temperatures recorded is also shown in Figure 5c. A plot with of the tabulated decay heat for the fuel inventory to be moved into dry storage is shown in Figure 6 (Mortenson, 2016).

Due to the close proximity of most of the reacting air with regards to the fuel, it is reasonable to use the on-contact calculations for dosage rates as a constant value throughout the canister as a conservative approximation. In ECAR 2906, MicroShield 9.01 was used to calculate the on-contact and 1-meter dosage rates for ATR fuel assemblies (Stewart 2012). Based on the decay heat for a given fuel assembly, the on-contact dosage rate can be estimated as

$$\dot{d} = 3.78 \times 10^{-3} Q, \tag{11}$$

in units of Gy/s, with Q as the decay heat rate given in Watts by

$$Q = Q_0 \exp\left(-0.023\ t_{year}\right) = Q_0 \exp(-7.2883 \times 10^{-10}\ t_{sec}\ ) \tag{12}$$

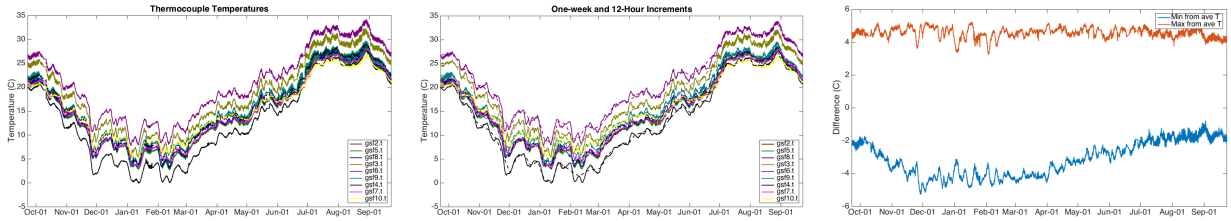

(a) (b) (c)

Figure 5. Thermocouple measurements over 1 year in the INL INTEC CPP-603 facility for (a) all one-hour recorded values, (b) twelve-hour and one-week increments, (c) maximum and minimum difference from average.

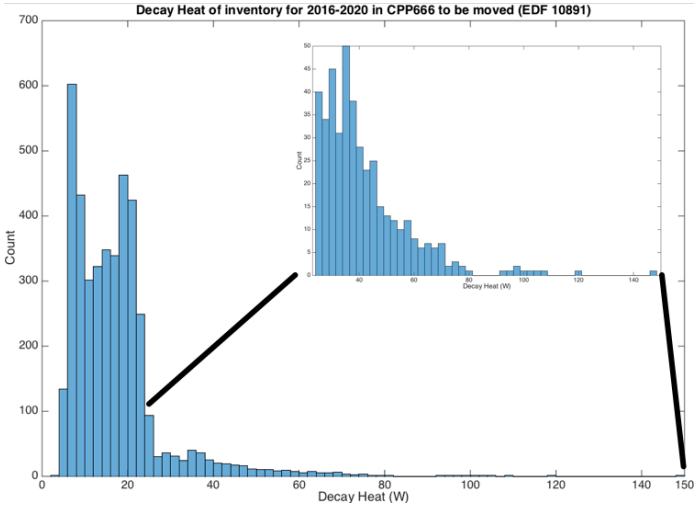

Figure 6. Histogram of the calculated decay heat of ATR fuel assemblies slated to be moved into dry storage.

2.5 Sensitivity Conditions

A wide range of model input parameters was studied to look at their effects of the peak fuel temperature and the maximum hydrogen concentration which could form over the course of a year in storage. The fuel decay heat was set to an average of 18 W, with a standard deviation of 12 W, values one standard deviation below, and two standard deviations above were set as the bounds (Mortenson, 2016). The dose rate was not used as a parameter, as it was assumed to be directly proportional to the decay heat (Stewart, 2012). The residual water in the sealed DOE standard canister was estimated in a previous report

(Wertsching, 2007) to be 0.032 to 0.123 moles depending on assumptions used. At ambient conditions, the number of moles of helium present in the backfill void space (445L calculated with the model geometry) would be about 18 moles, giving mole compositions for water vapor of 0.18% and 0.68%, low and nominal values were rounded from this to be 0.1% and 1% mole percent of water vapor. While this same report lists approximately 1.65 L of chemisorbed water through boehmite or gibbsite in the aluminum surface layers is possible, it is noted elevated temperatures would be needed for this to be released. It could be considered that the chemisorbed air is in saturated water vapor for a conservative upper limit. For an upper limit at a relative humidity of 100% for an average canister air temperature at 50C, the vapor pressure calculated with Antoine's equation is 12.4 kPa, and thus the mole fraction would be 9.9 %, with no condensation of water modeled. The pressure bounds were estimated based on safety reports analyzing the DOE standard canisters (Lockheed Martin 1998; Wertsching, 2007), higher pressure in the canister is assumed as the preferred condition as this shifts the equilibrium towards less hydrogen production. The exterior canister temperature fluctuates seasonally as shown previously in Figure 3. For the variation of this, the base case is the average of this plot, varied over time, the upper and lower bounds were set as conservative estimates on the range of the thermocouple data as ± 5 °C. The canister emissivity affects the amount of thermal radiation heat lost to the exterior air, a wide range of values are listed for stainless steel in the literature (Incropera et al., 2007), high canister emissivity is considered the preferred condition to promote more heat transfer loss for lower temperatures. The summary of these sensitivity parameters is listed in Table 3.

Table 3. *Parameter Sensitivity Ranges.*

Parameter	Lower Bound	Base Case	Upper Bound
Decay Heat [W]	6	18	42
Residual H2O [mol %]	0.1	1	10
Pressure [psig (Pa)]	5 (135798)	3.5 (125457)	2 (115114)
Exterior Temperature [°C]	Average -5	Average +0	Average +5
Canister Emissivity [-]	0.70	0.46	0.22

The initial modeling results utilizes 3 cases – lower bound for all, base case for all, and upper bound for all of the sensitivity parameters.

2.6 Time-stepping

One difficulty in this coupled approach in the long-term modeling of a spent nuclear fuel canister is that the restriction on the velocity inhibits the time steps due to the Courant number restriction is on the order of one-hundredth of a second, while a year of modeling requires 3.1 x 10^7 seconds. The transient response of the velocity along the centerline horizontal plane to a step change in the thermal field of the solid phases is shown in Figure 7a with 0.01 s timesteps, the velocity response to the step temperature change takes less than 5 seconds of simulated time to reach a new steady state velocity field. One way around the large number of timesteps required to simulated a year of physical time is the use of the segregated solver setting in STARCCM which allows for the velocity field to be frozen while still solving the coupled thermal and species transport equations. This brings in another limitation in the thermal energy limitation from the von Neumann restriction on thermal time steps. The response of the average fuel plate temperature to an exterior step change in ambient temperature is shown in Figure 7b for timesteps from 10s up to 900 s (15 minutes). At large timesteps, there is numerical error in the response time of the system due to the thermal diffusion rate across the volume cells, though at 100 s timestep the temperature is within one-tenth of a degree from time stepping at 10s. The energy equation is then frozen, and only the species equations are solved at the most extreme size of timesteps. The timesteps for the species solver are shown in Figure 8a-c for timesteps ranging from 10s to 1000s. At 1000s time steps, the long term trends of the species are in good agreement, and while some of the initial short-term peaks in chemical speciation may not be captured with the model, these peaks are likely inconsequential for the long term chemical modeling of the canister.

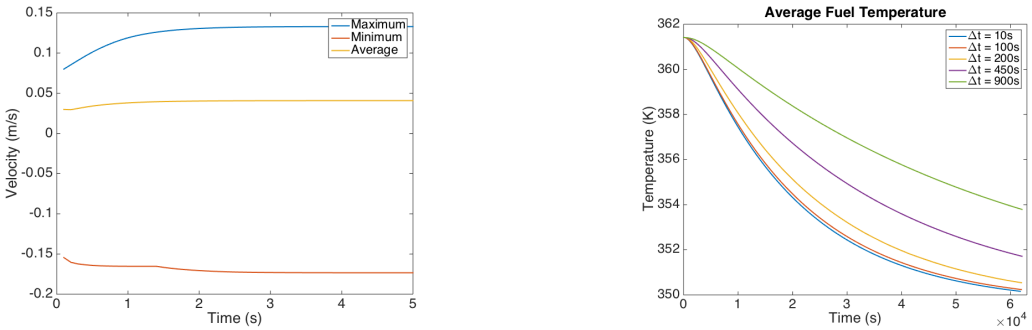

(a) (b)

Figure 7. The (a) velocity response on horizontal center line of canister to a change in thermal field (b) Temperature response of average fuel plate temperature to a change in external canister temperature.

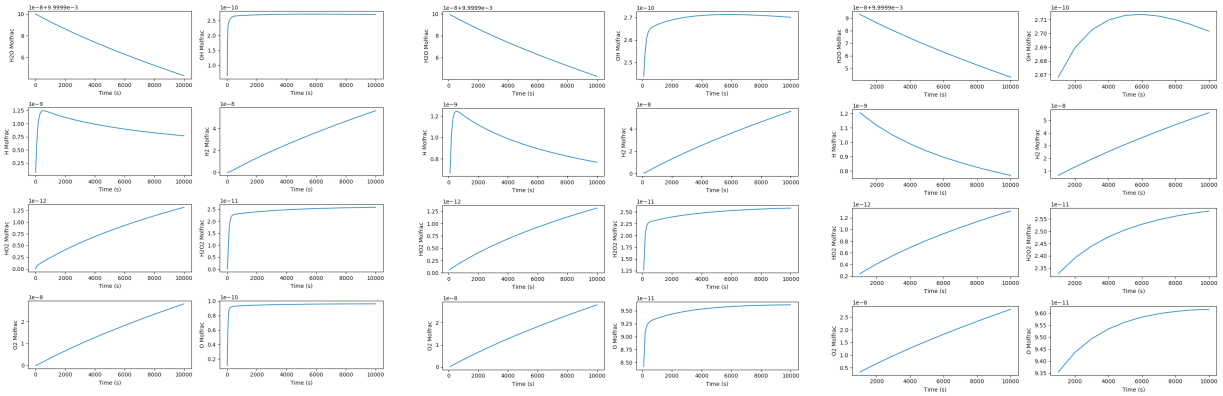

(a) (b) (c)

Figure 8. Cantera batch-reactor result with (a) 10s timesteps, (b) 100s timesteps and (c) 1000s timesteps.

Due to the long thermal response time seen in the thermal couples it is not necessary to update the thermal field that regularly. The initial temperature field is used as the converged iteration of the steady state case. The time-stepping scheme used is 3 seconds at 0.01 s with all equations enabled, 43200 s (12 hours) at 100 s with velocity field frozen, 561600 s (6.5 days) at 1000s with velocity field and energy equation frozen, 43200 s (12 hours) at 100 s with velocity field frozen, 561600 s (6.5 days) at 1000s with velocity field and energy equation frozen, 43200 s (12 hours) at 100 s with velocity field frozen, 561600 s (6.5 days) at 1000s with velocity field and energy equation frozen, 43200 s (12 hours) at 100 s with velocity field frozen, 561600 s (6.5 days) at 1000s with velocity field and energy equation frozen. This completes roughly 1 month of simulated time, then the velocity field is updated again, and this time-stepping procedure is repeated. This results in an algorithm that is 4276 timesteps to simulate one month of physical time. For clarity, Figure 9 shows a flow chart for the time stepping algorithm used.

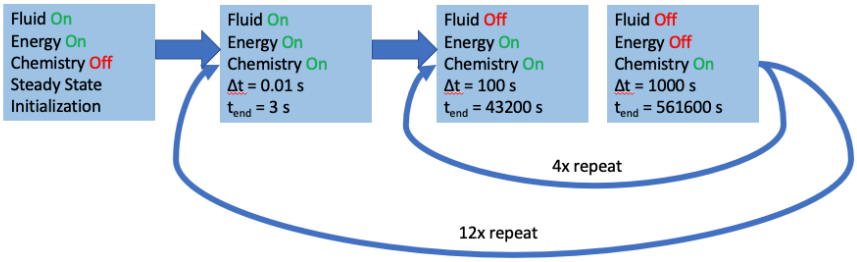

Figure 9. Flowchart showing the time stepping algorithm used in the CFD model.

2.7 Grid Convergence

The model was tested for spatial convergence, as well as some meshing options. The mesh used in the simulations has a base mesh size of 0.05 m, the Thin Mesher set to 2 cells across. For spatial convergence, the base resolution resulted in max, mean and minimum temperatures of 325.3, 318.2 and 299.7 K, respectively. The resolution was increased by a factor of $\sqrt{2}$ and 2, with base mesh sizes of 0.035 m and 0.025 m respectively, the results for the maximum, minimum and average temperatures are shown in Table 4. The change in the temperature was well under 1 °C across the profile so it deemed sufficient for the base case to have the resolution required. Figure 10 shows the refined meshes, here the medium refinement increased to 10.8 million cells, and the fine level increased to 21.3 million cells.

Table 4. *Summary of temperatures in different mesh sizes.*

Average Temperature [K]	Base Case	√2x higher resolution	2x higher resolution
Fuel	320.64	320.62	320.77
Basket	318.15	318.12	318.25
Canister	310.27	310.23	310.32
Air	318.21	318.17	318.32
Maximum Temperature [K]			
Fuel Max	325.32	325.29	325.45
Basket Max	323.53	323.51	323.66
Canister Max	314.16	314.21	314.32
Air Max	325.32	325.29	325.46
Minimum Temperature [K]			
Fuel Min	315.21	315.18	315.28
Basket Min	307.86	307.85	307.91
Canister Min	299.70	299.65	299.67

Air Min	304.64	304.45	304.51

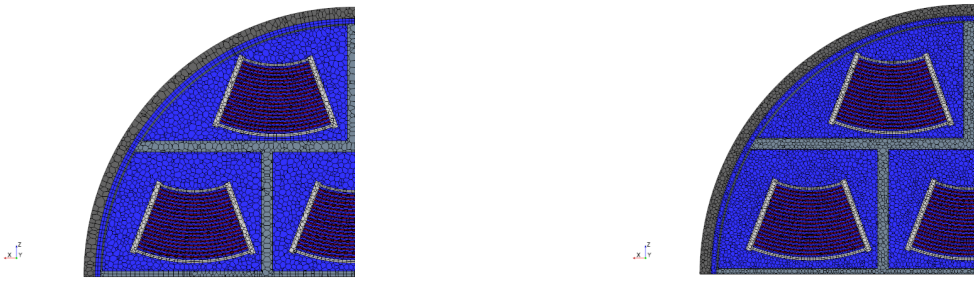

(a) (b)

Figure 10. A horizontal slice of the (a) medium and (b) finest mesh parameters considered.

In addition, increasing the number of thin mesh layers up to 3 and 4 was also tried as a meshing option with minimal change in results. While it is recognized a coarser mesh could be used, the meshed geometry of the fuel plates became more trapezoidal in nature when this was attempted, and while temperature profiles were similar, the resulting visualizations were showed unnatural fuel shapes.

A grid convergence index (GCI) is utilized, from Oberkampf and Roy 2010, given by

$$GCI = \frac{F_s}{r^p - 1}\left|\frac{f_2 - f_1}{f_1}\right| \tag{13}$$

where F_s is the factor of safety, equal to 1.25, r is the mesh size ratio, p is the order, which is 2 for these cases, and f is the solution value for the cases. Using this, then the average GCI for the mesh used in these simulations compared to the medium refined mesh in 0.05%, and the average GCI from the medium to high resolution is 0.01%. These results show the meshing parameters used for the sealed canister geometry should be sufficient for the study.

3. RESULTS AND DISCUSSION

3.1 Thermal Field

Figure 11 shows the thermal profile for lower, central and upper Type 1a baskets within the canister for the updated steady state parameter cases for the low, nominal and high end. The maximum, average and

minimum values are summarized in Table 5. Hotter regions occur in the center ATR fuel assembly with colder regions at the canister walls. The central basket shows higher temperatures than the upper and lower baskets.

Table 5. *Summary of temperatures for updated steady-state cases.*

Case	Max T [C]	Average Fuel T [C]	Average Air T [C]	Minimum Fuel T [C]	Minimum Air T [C]
Low	26.2	24.6	23.6	22.8	19.2
Base	49.9	44.9	42.7	39.7	29.7
High	95.4	84.6	78.8	71.2	48.6

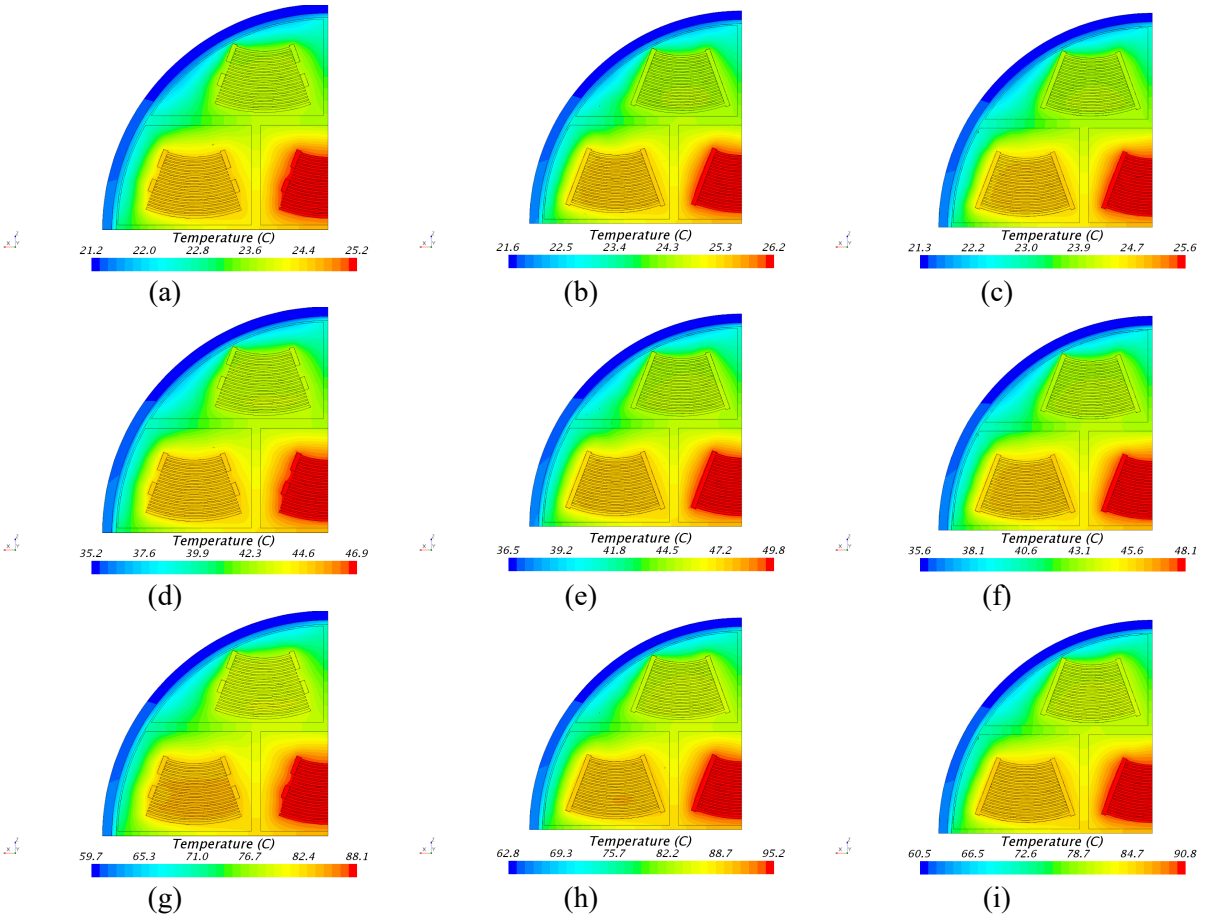

Figure 11. The temperature for the low case: (a) lower, (b) central, (c) upper horizontal plane; nominal case: (d) lower, (e) central, (f) upper horizontal plane; and upper case (g) lower, (h) central, (i) upper horizontal plane.

The nominal case was completed for a month of simulated time using the time stepping procedure that was outlined in section 2.6. Figure 12a shows the development of the average, minimum and maximum temperatures for the inner air and fuel during the period, and Figure 12b shows the development of the

outer temperatures for the canister and Type 1a baskets. As expected with the slow development of the exterior temperature that was shown in Figure 7, the temperature of the interior components of the canister does not drastically change over a month long period.

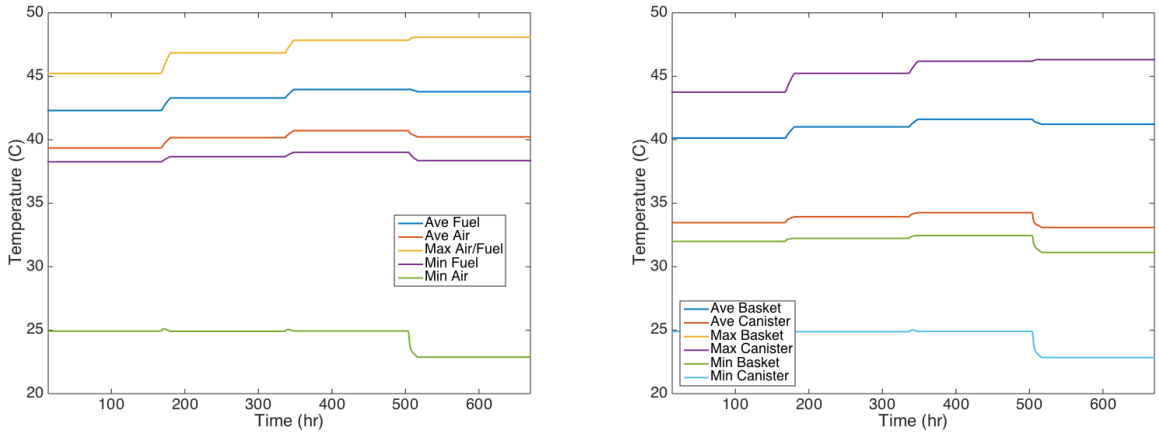

Figure 12. The change in the average, minimum and maximum temperatures over a one-month simulation for (a) fuel and interior air and (b) canister and baskets.

3.2 Velocity Field

Figure 13 shows the y-velocity component at lower central and upper horizontal locations within the canister. As expected, the largest regions of downwards flow are in the cooler edges of the canister, and hotter regions show upwards flow. The air gaps within the fuel plates show rather negligible flow rates. Due to the slots the run the length of the basket that are in the Type 1a container, each slot has its own circulation pattern, rather than a global circulating pattern.

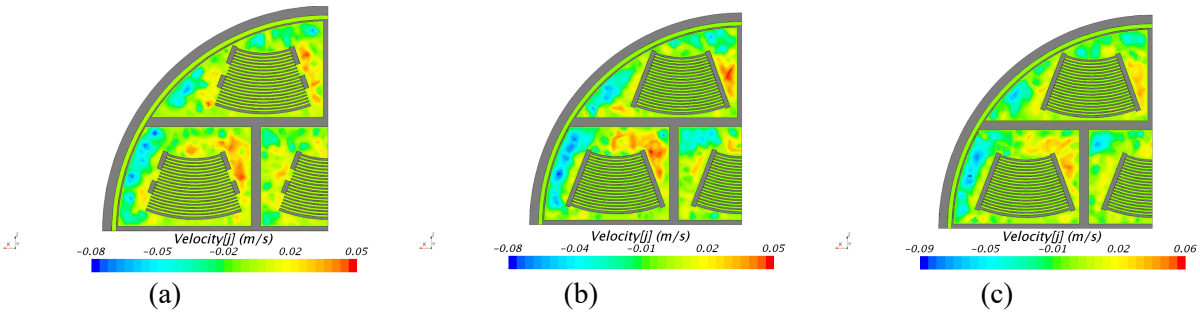

Figure 13. Y-Velocity slice for the (a) lower, (b) center and (c) upper cross sections.

3.3 Chemical Field

Figure 14 shows the concentration profile of hydrogen within the canister, which changes based on the local temperatures. The hottest regions of the storage canister show the lowest value of hydrogen concentration, which a spatial variation of about 20%. The small air gap between the outer diameter of the basket and the inner diameter of the canister shows the highest hydrogen concentration. At higher temperatures, the chemical reaction system trends more towards the reactions which consist of the recombination of radicals back into water vapor rather than hydrogen- which is the cause of higher outer concentrations, and lower central concentrations.

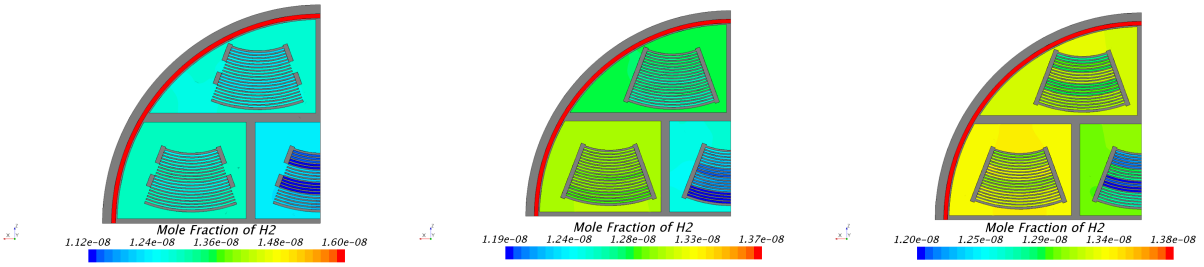

(a) (b) (c)

Figure 14. Horizontal slices of the hydrogen mole fraction after one-month for (a) lower, (b) central and (c) upper baskets.

The concentrations of hydrogen and other species can be tracked with this coupled CFD + radiolytic chemistry model. Figure 15 shows the spatially averaged mole fraction of hydrogen, HO_2, O, OH, and H over a month-long period. Most species reach near an equilibrium level rather quickly, then the hydrogen and hydroperoxyl continue to show a steady production rate, though hydroperoxyl is orders of magnitude less and could be negligible in long term runs. This result is in line with batch reactor-Cantera results, as well as previous work (Wittman & Hanson, 2015) that show in the absence of residual air, only very trace amounts of hydrogen production would be expected.

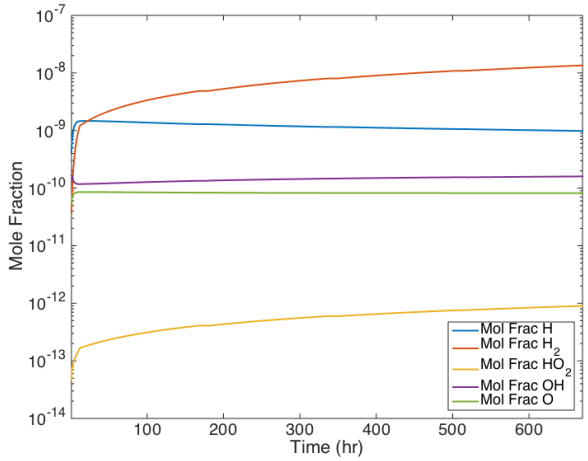

Figure 15. Semi-log Plot of the spatially-averaged concentration of hydrogen and other minor species.

4. CONCLUSIONS AND FUTURE WORK

A 3D coupled CFD with chemical radiolysis model of a sealed DOE standard canister was successfully developed. This model has demonstrated the ability to show a transient solution for the thermal field and chemical species over long simulation time periods for extended storage applications. A workflow for systematic reduction of complex radiolysis reaction network within sealed canister was established.

For the sensitivity parameters of the model that have been identified, additional simulations will test one-at-a-time sensitivity values to the quantities of interest such as maximum temperatures and hydrogen concentration as well as cross-correlation between the parameters. The model presented here currently uses constant dose rates. This will be updated in the future with MCNP simulation results to contain spatially varying dose rates to be used for the radiolytic chemistry kinetic rates.

The next steps are to extend this procedure to develop 3D coupled CFD + radiolysis models for the unsealed, vented canister storage system subjected to episodic breathing using INL INTEC CPP-603 facility as the model storage system. The unsealed and vented canisters will contain air rather than helium, so the full chemical mechanism should be substantially increased in complexity, but we believe the same workflow for reaction network reduction developed would also be applicable for the unsealed system. As data becomes available from the experimental work, the chemical mechanism in the model will be updated.

REFERENCES

Arkhipov, O.P., Verkhovskaya, A.O., Kabakchi, S.A., and Ermakov, A.N., 2007. Development and verification of a mathematical model of the radiolysis of water vapor. Atomic Energy, 103(5):870.

Atkinson, R., Baulch, D.L., Cox, R.A., Crowley, J.N., Hampson, R.F., Hynes, R.G., Jenkin, M.E., Rossie, M.J., and Troe, J., 2004. Evaluated kinetic and photochemical data for atmospheric chemistry: volume I – gas phase reactions of X, HOx, NO2, and SOx species. Atmospheric Chemistry and Physics, 4(6): 1461-1738.

Bang, K.-S., Yu, S.-H., Lee, S.-H., Lee, J.-C., Seo, K.-S., 2015. Experimental investigation of heat removal performance of a concrete storage cask. Annals of Nuclear Energy 85, 679–686.

Brewster, R. A., Baglietto, E., Volpenhein, E., Bajwa, C. S., 2012. Cfd analyses of the tn-24p pwr spent fuel storage cask. In: ASME 2012 Pressure Vessels and Piping Conference. American Society of Mechanical Engineers, pp. 17–25.

Bulearca, A.M., Calinescu, I., and Lavric, V., 2010. Model Studies of NOx and Sox reactions in Flue gas treatment by electron beam. UPB Sci Bull, Series B, 72(1):101-112.

Christensen, A., 2003a. EDF-2760, The Irradiated Fuel Storage Facility Maximum Heat Load And Resulting Maximum Temperatures When the Ventilation System Is Not Operating. Tech. rep., Idaho National Laboratory.

Christensen, A., 2003b. EDF-5579 Corrosion Potential of the Irradiated Fuel Storage Facility Environment. Tech. rep., Idaho National Laboratory.

Goodwin, D.G., Moffat, H.K., and Speth, R.L. Cantera: An object-oriented software toolkit for chemical kinetics, thermodynamics, and transport processes. http://www.cantera.org, 2017. Version 2.3.0. doi:10.5281/zenodo.170284

Heng, X., Zuying, G., Zhiwei, Z., 2002. A numerical investigation of natural convection heat transfer in horizontal spent-fuel storage cask. Nuclear Engineering and Design 213 (1), 59–65.

Herranz, L. E., Penalva, J., Feria, F., 2015. Cfd analysis of a cask for spent fuel dry storage: Model fundamentals and sensitivity studies. Annals of Nuclear Energy 76, 54–62.

Illum, D.B., 1996. ATR Fuel Summary Report. Tech. Report INEL-96/300.

Incropera F.P., DeWitt ,D.P. , Bergman, T.L. and Lavine, A.S., 2007. Fundamentals of Heat and Mass Transfer, Sixth Edition, John Wiley and Sons, Hoboken, NJ.

Jeong, Y. S., Bang, I. C., 2016. Hybrid heat pipe based passive cooling device for spent nuclear fuel dry storage cask. Applied Thermal Engineering 96, 277–285.

Kim, H., Kwon, O. J., Kang, G.-U., Lee, D.-G., 2014. Comparisons of prediction methods for peak cladding temperature and effective thermal conductivity in spent fuel assemblies of transportation/storage casks. Annals of Nuclear Energy 71, 427–435.

Kim, S. S., Pope, C., Taylor, L. L., et al., 2007. Criticality analysis for proposed maximum fuel loading in a standardized snf canister with type 1a baskets, INL/EXT-07-12326. Tech. rep., Idaho National Laboratory.

Lee, D.-G., Park, J.-H., Lee, Y.-H., Baeg, C.-Y., Kim, H.-J., 2013. Natural convection heat transfer characteristics in a canister with horizontal installation of dual purpose cask for spent nuclear fuel. Nuclear Engineering and Technology 45 (7), 969–978.

Lee, J., Choi, W., Bang, K., Seo, K., Yoo, S., 2009. Thermal-fluid flow analysis and demonstration test of a spent fuel storage system. Nuclear Engineering and Design 239 (3), 551–558.

Lee, S. Y., Sindelar, R. L., Losey, D. C., 2000. Thermal modeling and performance analysis of interim dry storage and geologic disposal facilities for spent nuclear fuel. Nuclear technology 131 (1), 124–151.

Li, J., Liu, Y. Y., 2016. Thermal modeling of a vertical dry storage cask for used nuclear fuel. Nuclear Engineering and Design 301, 74–88.

Lockheed Martin Idaho Technologies Co, Idaho National Engineering and Environmental Lab, Idaho Falls, ID (United States) (Aug 1998). Preliminary design specification for Department of Energy standardized spent nuclear fuel canisters Volume 1: Design specification (DOE/SNF/REP--011-Vol 1). United States

Mortensen, K., 2016, EDF-10891, Decay Heat of ATR Elements to be Transferred from CPP-666 FSA to IFSF, Tech. rep., Idaho National Laboratory.

Nishimura, M., Shibazaki, H., Fujii, S., Maekawa, I., 1996. Natural convection heat transfer in the horizontal dry storage system for the lwr spent fuel assemblies. Journal of nuclear science and technology 33 (11), 821–828.

Oberkampf, W.L., and Roy, C.J., 2010, Verification and Validation in Scientific Computing, Cambridge Univeristy Press, Cambridge, NY.

Polkinghorne, S.T. and Lacy, J.M., 1991. Thermophysical and Mechanical Properties of ATR Core Materials, Report No. PG-T-91-031, EG&G Idaho Inc.

Poˇskas, R., Sˇimonis, V., Poˇskas, P., Sirvydas, A., 2017. Thermal analysis of castor rbmk-1500 casks during long-term storage of spent nuclear fuel. Annals of Nuclear Energy 99, 40–46.

Siemens, 2017. Star-ccm+ v12.06.08r-12.

Smith, B. L., 2016. Validation experiments for spent-fuel dry-cask in-basket convection. Tech. rep., Utah State Univ., Logan, UT (United States).

Solis, J., Zigh, G., 2016. Impact of variation in environmental conditions on the thermal performance of dry storage casks, nureg-2174. Tech. rep., U.S. NRC.

Solıs, J., Zigh, G., 2017. Best practice guidelines for the use of cfd in dry cask applications.

Stewart, D., 2012, ECAR-2906. ATR Fuel Element In-Air Dose Rate Estimates Base on Heat Generation, Tech rep., Idaho National Laboratory.

Takeda, H., Wataru, M., Shirai, K., Saegusa, T., 2008. Development of the detecting method of helium gas leak from canister. Nuclear Engineering and Design 238 (5), 1220–1226.

Tseng, Y., Lin, C., Shih, C., Wang, J., 2016. Evaluating the feasibility of new surveillance concept for dry storage system through cfd methodology. Nuclear Engineering and Design 304, 1–10.

Tseng, Y.-S., Wang, J.-R., Tsai, F. P., Cheng, Y.-H., Shih, C., 2011. Thermal design investigation of a new tube-type dry-storage system through cfd simulations. Annals of Nuclear Energy 38 (5), 1088–1097.

Wertsching, A.K., Hill, T.J., Mackay, N. and Birk, S.M., 2007. Material Interactions on Canister Integrity During Storage and Transport. Tech. rep. Idaho National Laboratory, DOE/SNF/REP-104.

Wittman, R., Hanson, B., 2015. Radiolysis model analysis for a used fuel storage canister. In: IHLRWM April 2015.

Wu, Y., Klein, J., Zhou, H., Zuo, L., 2018. Thermal and fluid analysis of dry cask storage containers over multiple years of service. Annals of Nuclear Energy 112, 132–142.

Yoo, S. H., No, H. C., Kim, H. M., Lee, E. H., 2010. Full-scope simulation of a dry storage cask using computational fluid dynamics. Nuclear Engineering and Design 240 (12), 4111–4122.

Zigh, G., Solis, J., 2013. Computational fluid dynamics best practice guidelines for dry cask applications, nureg-2152. Tech. rep., U.S. NRC.